Granular flows : fluidization and anisotropy
Wortel, G.H.

Cover Page

Universiteit Leiden

Author: Wortel, Geert
Title: Granular flows : fluidization and anisotropy
Issue Date: 2015-11-19

VIBRATION DOMINATED FLOW IN WEAKLY VIBRATED GRANULAR MEDIA

In this chapter we describe the rheology of weakly vibrated granular flows as function of flow rate, vibration strength and pressure, by performing experiments in a vertically vibrated split-bottom shear cell[1]. For slow flows, we establish the existence of a novel vibration dominated granular flow regime, where the driving stresses smoothly vanish as the driving rate is diminished. We distinguish three qualitatively different vibration dominated rheologies within this slow flow regime, most strikingly a regime where the shear stresses are no longer proportional to the pressure.

3.1 Introduction

In chapter 2 we described how the rheology of weakly vibrated granular media reveals a variety of qualitatively different flow regimes. First, for large flow rates, inertial effects dominate, and the effect of vibrations is small. Second, for intermediate flow rates, we cross over to a regime similar to the well-known quasi-static flows that have been studied at length in the absence of vibrations [71, 76–79, 94]. Third, for even slower flows, we enter a regime where the vibrations lead to completely new rheological behavior.

The focus of this chapter is on these *vibration dominated flows*. By probing the equilibration times of the stresses and the variation of the steady state stresses with filling height, we find evidence for three qualitatively

---

[1]G. Wortel, J. Dijksman, and M. van Hecke, *Rheology of weakly vibrated media*, Phys. Rev. E **89**, 012202 (2014) [81]

different regimes. For slow enough flows, vibration effects increasingly dominate the physics, leading to compaction of the material for weak vibrations, and to fluidization of the material for vibrational accelerations approaching gravity. Most strikingly, in the latter regime, we see a breakdown of the proportionality of shear stresses and pressure, a highly unusual phenomenon in granular flows.

The outline of this chapter is as follows. In Sec. 3.2 we describe the measurement protocols used in the current and previous study [71]. In Sec. 3.3 we describe the main phenomenology of a complete set of experiments probing $T(\Gamma, \Omega, h)$. In Sec. 3.4.1 we introduce the canonical perspectives on granular rheology, including a model for the stresses in split-bottom flows by Unger *et al.* [95]. In Sec. 3.4.2 we use this model to extract effective friction coefficients from our data, as well as exploring the quality of the fit between the data and this model. In Sec. 3.4.3 we provide strong evidence for the existence of a pressure-independent flow regime though measurements of the flow structure.

3.2 Protocol

In this section we discuss our measurement protocols, and show how we ensure that we measure steady values for the rheology.

Our experiments focus on the rheological curves which relate the driving torque T and the driving rate Ω. Our main focus is on experiments where we fix the driving rate in the range from 10^{-4} to 1 rps, and probe the torque. We perform these experiments for a range of vibration amplitudes $\Gamma = 0, 0.2, 0.5, 0.7, 0.83, 0.95$ and 1, and moreover use seven different filling heights ($h = 0.19, 0.25, 0.31, 0.38, 0.44, 0.50$ and 0.56). Varying h allows us to probe the role of the confining pressure for the rheology.

Each experiment starts with switching on the vibrations, after which we allow the shaker feedback loop 30 s to settle to the required value of Γ. We proceed by applying an amount of preshear to the granular material, in order to obtain similar starting conditions for each experiment. Unless noted otherwise, the protocol consists of the following steps: *(i)* 2 s of 1 rps rotation clockwise; *(ii)* 4 s of 1 rps rotation counter-clockwise; *(iii)* 2 s of 1 rps rotation clockwise. *(iv)* 5 s without imposed stress or shear. *(v)* start of actual measurement. The rotation in the experiments is in the clockwise direction to minimize anisotropy effects [96].
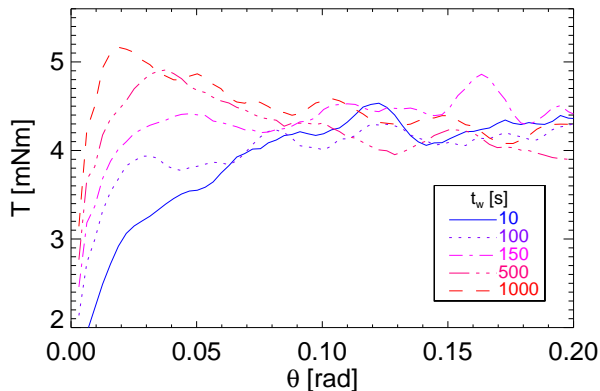
FIGURE 3.1: The torque as function of deflection angle θ for $\Omega = 10^{-4}$ rps, $\Gamma = 0.7$, and $h = 0.31$, but different waiting time t_w between the preshear and the actual measurement.

Vibrations lead to compaction of granular media, although this process is very slow for $\Gamma < 1$ [58], whereas flow typically leads to dilatation [18]. Additionally, anisotropy in the fabric of the granular media needs a finite amount of strain to build up, but may be relaxed by vibrations [47, 96]. For both density and anisotropy, vibrations and flow are in competition, and as we are interested in steady state flow properties, we need to ask: what is the minimum time or strain necessary to get into a steady state flow regime?

We have probed the relaxation of our flows to a steady state by starting the flow from a denser or less densely packed state as follows: before each experiment, we perform preshear as described above. After preshear, during stage *(iv)*, we stop the shear and vibrate the material for a waiting period t_w, during which the granular packing density increases by compaction, and then start the actual measurements. By varying the t_w, we thus manipulate the packing fraction at the start of the flow. By measuring the torque as function of time we capture the evolution of the torque to its steady state value. As we expect this equilibration to be slowest for small Ω we perform this test at the smallest Ω (10^{-4} rps) that we explore in our experiments. The results of this test are shown in Fig. 3.1, where we plot T as function of the total angle of rotation of the bottom disk θ.
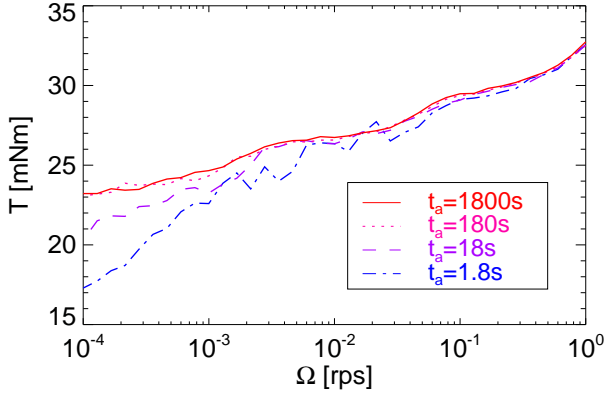
21

FIGURE 3.2: Flow curves for different averaging times t_a. Below $\Omega \approx 0.5 \times 10^{-3}$ rps, the torque increases with the waiting time. The measurements are for $\Gamma = 0.6$ and $h = 0.56$.

This figure shows that for small t_w, T grows monotonically before reaching steady state, whereas for large t_w, the torque peaks at values larger than the steady state value. This is consistent with a simple picture where the longer the waiting time, the denser the grains are packed at the start of the experiment, and the larger the torque needed to cause flow.

For all waiting times, the torque reaches its steady state value for $\theta < 0.1$ rad, corresponding to a measurement time of 150 s at 10^{-4} rps. We claim that this represents the longest equilibration time necessary to reach a steady state flow situation, as all our experiments are carried out for $\Omega \geq 10^{-4}$ rps. Moreover, in many experiments our data is acquired in a so-called strain rate sweep, where the rotation rate is varied by a small amount so that equilibration will be faster. In all cases, an equilibration strain or time of $\theta > 0.1$ rad, or 150 s, will be sufficient to obtain steady state flow curves. We choose 180 s for all the experiments described in this chapter. Additional data that supports the claim that, also for lower Γ, a new steady state is reached within $\theta < 0.1$ rad, can be found in Ref. [13].

To independently verify that equilibration times of 180 s are long enough, we perform a strain rate sweep at fixed $\Gamma = 0.6$. We sweep the flow rate from fast to slow rates, and then compare flow curves obtained for different times t_a per step, as shown in Fig. 3.2. While for small values of Ω
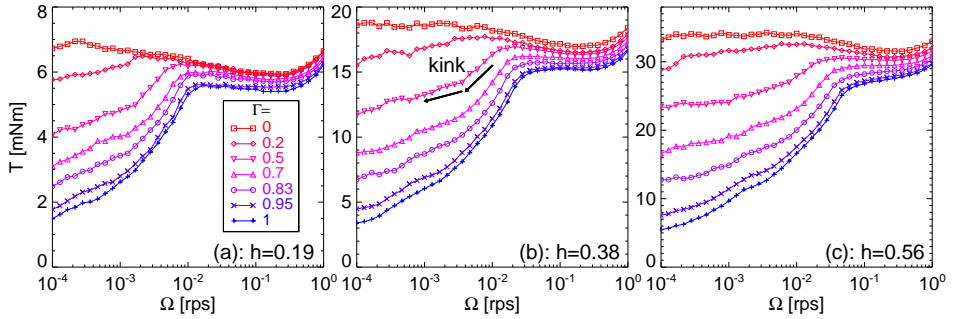
FIGURE 3.3: Selected flow curves for fixed filling height and varying Γ. In all cases, T decreases monotonically with Γ– its dependence on Ω is more complex. The selected filling heights are $h = 0.19$ (a), $h = 0.38$ (b), $h = 0.56$ (c).

and t_a, the torque shows a variation with t_a, for all the flow rates probed here we note that the data for $t_a = 180$ s and 1800 s are indistinguishable, showing that for $t_a \geq 180$ s the obtained values of T are steady state values. As a final additional test, we have also inspected $T(t)$ to confirm we reach steady state [13].

3.3 Phenomenology

We now turn our attention to the rheological curves $T(\Omega)$. As shown in the $T(\Omega)$ curves in Fig. 3.3, the flows in our system exhibit a rich rheology. There are two simple trends we see illustrated in these curves: increasing the filling height always increases T, whereas increasing the vibration strength always decreases T. The role of the flow rate is not as simple, with the torque often being a non-monotonic function of the disk rate Ω– moreover, the details of the rheological curves depend on both the vibration strength Γ and filling height h. We note here that the sign of $\partial T/\partial \Omega$ has a crucial rheological implication: flows for which $\partial T/\partial \Omega > 0$ can also be accessed in experiments where the torque is fixed, whereas flows for which $\partial T/\partial \Omega < 0$ are *unstable* in torque-controlled experiments. As we discussed in [71], this range of unstable flows leads to hysteretic switching between two different flow regimes when the torque is varied, and is deeply connected to the yielding behavior of granular media observed for $\Gamma = 0$.

Here we focus on rate-controlled experiments, and as a first step in characterizing these curves, we plot the boundaries between the regions where $\partial T/\partial \Omega$ is positive and negative for three values of h in Fig. 3.4. Roughly speaking, we can distinguish three regimes.

Inertial flows — For $\Omega \gtrsim 0.3$ rps, $\partial T/\partial \Omega > 0$; the flow curves show an increasing T for increasing Ω. This increase corresponds to the onset of the inertial regime [93]. To estimate the inertial number $I = \dot{\gamma} d/\sqrt{P/\rho}$ at $\Omega = 0.3$ rps, we have to choose a characteristic pressure and strain rate scale, as both $\dot{\gamma}$ and P vary throughout the system. Taking P as the hydrostatic pressure at $0.5H$, and $\dot{\gamma}$ corresponding to a shear band of three particles wide, we get $I = 0.09$ for $h = 0.38$ and $\Omega = 0.3$ rps. Considering that the inertial regime typically starts at $I = 0.1$ [90], there is good agreement between the onset of increasing $T(\Omega)$ and the onset of the inertial regime. In the remainder of the chapter we will focus on slower flows.

Unstable flows — For intermediate flow rates, $T(\Omega)$ has a negative slope for small Γ – for $\Gamma \to 0$, this regime extends to arbitrarily small flow rates, although there the flow curves become essentially flat. Despite the unsta-
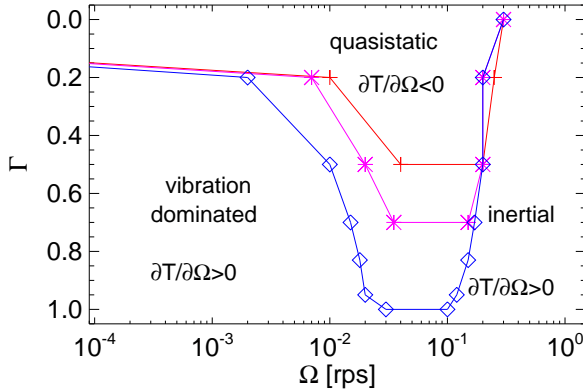

FIGURE 3.4: The boundaries between the regions where the flow curves have a positive and a negative slope for $h = 0.19$ ($\diamond$), $h = 0.38$ ($*$) and $h = 0.56$ ($+$). For $\Gamma = 0$ and $\Omega < 0.3$ rps, the flow curve always has a negative slope. The region extends to $\Gamma > 0$, and it extends to higher Γ for lower h.

ble character of the global rheology, and in contrast to unstable flows in *e.g.* micelles [61], we do not see any changes in the shear bands as we move in and out of this unstable regime. As the variation of the stress with flow rate is not very large, this regime can also be referred to as *quasi-static*.

Vibration dominated flows — Both the unstable/quasi-static and inertial regime have been studied in great detail already [36, 37, 66, 90, 94, 97], as they also arise in the absence of vibrations. Hence, in the remainder of the chapter we will focus on the new vibration dominated regime of slow, stable flows that arises for $\Gamma > 0$ and $\Omega < 10^{-2}$ rps.

One striking qualitative feature of this regime we already want to point out is the pronounced "kink" in the flow curves that can be seen for $10^{-2} < \Omega$ [rps] $< 10^{-3}$ in Fig. 3.3. In Fig. 3.3(b) we explicitly mark such a kink. The kinks coincide with the flow rates where t_a needs to be sufficiently large for T to equilibrate (see Fig. 3.2). We suggest that at sufficiently low Ω, compaction effects become significant, leading to an increase of T with time, and a "kink" in the flow curves.

3.4   Vibration Dominated Flows

We will now turn our attention to the increase of T with h, which allows us to probe the underlying mechanisms that govern the rheology of vibration dominated flows. The canonical starting point of descriptions of *non-vibrated* slow granular flows is that the shear stresses τ are proportional to the pressure P [66, 94, 97], and the ratio of τ and P is an effective friction coefficient, μ. For inertial flows, a description where μ becomes rate dependent (through the inertial number) has been shown to capture much of the phenomenology [36, 37, 90], and for slow, non-vibrated flows, this Mohr-Coulomb picture combined with a non-local rheology captures the essentials of steady, slow granular flow [68–70].

By varying the filling height h, we can modify the pressure P and probe its role for the rheology in the different regimes. Here, we do not measure P, but assume it to be hydrostatic. Clear predictions for $T(h)$ exist from a well-studied rheological model for the driving torques in a split-bottom geometry [95]. In addition, this model provides clues to the flow's spatial structure and how it depends on friction and other factors. In this section, we describe how our experiments allow us to build on these

basic ingredients to identify two qualitatively different regimes in vibration dominated flows. We find a frictional regime in which $P \sim \tau$, yet with $\mu(\Omega)$ a rate-dependent friction for $\Omega \gtrsim 10^{-3}$ rps or $\Gamma \lesssim 0.8$. For even slower, more strongly vibrated flows, both the rheology and the location of the shear band presents strong evidence for a regime where T becomes *independent* of P.

3.4.1 Torque Minimization Model

To interpret the observed filling height dependence of the shear stresses, we start from a simple frictional model due to Unger *et al.*, which was developed to describe the three-dimensional shape of the shear zones in the split-bottom geometry, but which also makes a precise prediction for the driving torque as function of filling height for purely frictional flows [76, 77, 95]. This model is based on the following three ingredients. First, think of the shear zones as localized along a narrow sheet $r(z)$ (corresponding to the center of the shear zones [76–79]). Second, assume that the stress tensor is collinear with the strain rate tensor [66] and proportional to the hydrostatic pressure. Third, assume that the sheet shape $r(z)$ minimizes the driving torque[2]:

$$\tilde{T}[r(z)] = 2\pi g \rho \mu \int_0^H (H - z)\, r^2 \sqrt{1 + (dr/dz)^2}\, dz \,, \qquad (3.1)$$

where g denotes the gravitational acceleration, and ρ the bulk density $(1.7 \times 10^3$ kg/m$^3)$ of the granular material. Minimizing $\tilde{T}$ for a given h determines the shear sheet $r(z)$, from which the torque can be determined as function of h. As expected, we can write this torque as $\tilde{T}(h) = \mu \tilde{T}_f(h)$, where $\tilde{T}_f$ is a universal function of h. Note that for shallow filling heights, the torque is approximately proportional to the product of pressure and the extension of the shear band, so that $\tilde{T}_f(h)$ is quadratic in h for $h \ll 1$.

In contrast to the original split-bottom cell for which Eq. (3.1) was developed, in our system the driving disk is slightly elevated with respect to the bottom. This is done in order to avoid observing spurious torque fluctuations that we associate with the diverging strain rate in the original split-bottom setup. We have found that the torques occasionally show

---

[2]Note that whereas we characterize the filling height with the dimensionless h, we write the frictional model in terms of H, which is the common notation.
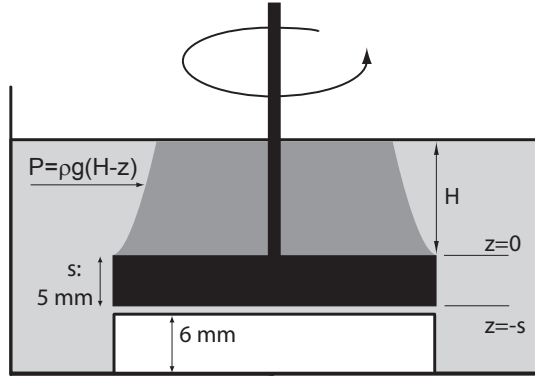
FIGURE 3.5: Schematic side view of the split-bottom setup. A cylinder of height 6 mm is placed underneath the disk, which has a thickness s of 5 mm and a radius r_s of 40 mm. The gray area represents the volume occupied by the grains; the dark gray region indicates the volume of particles corotating with the disk in the trumpet regime. The hydrostatic pressure P acts on the interface between the corotating and 'static' volume of particles as indicated. The side of the disk is also exposed to particles and, although smooth, contributes to dissipation during rotation as discussed in the text.

strong fluctuations in this case, presumable due to individual particle being trapped just above the split – moreover, these fluctuations depend on the precise roughness near the split, thus leading to a dependence of the average T on such experimental details. To avoid this, we make sure that the strain rate field is smooth at the grain level and have elevated the driving disk by 6 mm – see Fig. 3.5. The side of the disk is smooth, and particles immediately next to the disk hardly move, creating a static bottom layer flush with the disk. Hence, the boundary conditions are essentially the same as for the ordinary split-bottom disk, and the elevation does not affect the overall flow field for $h \equiv H/r_s$ larger than about 0.1. The elevation does ensue that the torques are insensitive to experimental details and do not show the aforementioned spurious fluctuations.

The elevated disk does lead to a μ-dependent addition in the experimental torque signal T, due to slip between the side of the disk and the
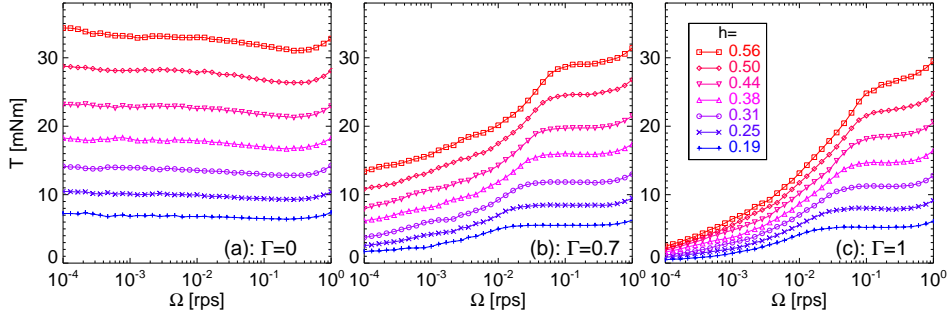
FIGURE 3.6: Selected flow curves for fixed Γ and varying h. In all cases, T grows monotonically with h. The selected values of Γ are: (a) $\Gamma = 0$, (b) $\Gamma = 0.7$ and (c) $\Gamma = 1$.

stationary particles next to it. This drag term can be estimated as:

$$T_{\text{drag}}(H) = 2\pi r_s^2 \mu \rho g \int_0^s (H + z)dz \ , \tag{3.2}$$

where s is the disk thickness (5 mm), and μ is the effective friction coefficient for sliding of the disk past the particles, for which we use the same effective friction coefficient as for the granular flow. The contribution of T_{drag} to the torque varies with H and is proportional to μ, so that we can write $T_{\text{drag}} = \mu T_d$, where T_d can be deduced from Eq. (3.2).

We conclude that the measured torque T is composed of two contributions:

$$T = \tilde{T}(H) + T_{\text{drag}} = \mu \left[\tilde{T}_f(H) + T_d \right] = \mu T_f \ , \tag{3.3}$$

so that, we can extract $T(h)$ from our flow curves, and check whether the flow appears frictional, and if so, determine μ [80] and $\tilde{T}(h)$.

Γ=0

In Fig. 3.6(a) we show flow curves for $\Gamma = 0$ and a range of h. Clearly, the torque only weakly varies with Ω and we expect the stresses to be frictional. For each fixed Ω, we extract $T(h)$ from our data and fit it to μT_f (Eq. (3.3)), as shown in the inset of Fig. 3.7. We find that this fit is excellent, which implies that the stresses are frictional, and which allows us to extract $\mu(\Omega)$. As shown in Fig. 3.7, $\mu(\Omega)$ is almost flat, and has the
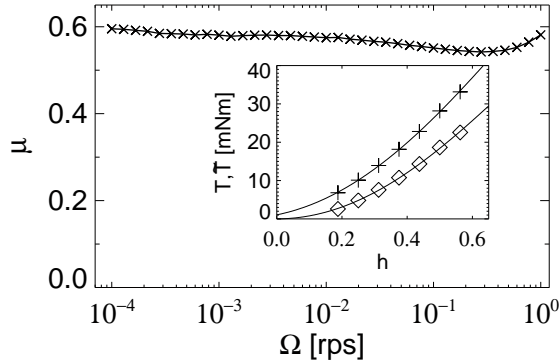
FIGURE 3.7: $\mu(\Omega)$ as obtained from the fit with the frictional model. The inset shows one example of the fit for $\Omega = 8.5 \times 10^{-4}$ rps. The upper curve (+) shows the raw data T, the bottom curve ($\diamond$) is the raw data minus the correction term, $\tilde{T}$ – which goes through the origin. The fit matches the data very well resulting in a χ^2 of 2.0×10^{-3} for the upper curve (see Eq. 3.4).

same shape as the flow curves. We stress here that $\mu(\Omega)$ together with the frictional model predicts the stresses for *all* values of h, thus representing all the flow curves taken at different h. We note that our values for μ are comparable to those found previously in a standard split-bottom cell using the same particles [76].

3.4.2 Frictional Model for $\Gamma > 0$

In Fig. 3.6(b) and Fig. 3.6(c) we show examples of flow curves for a range of h and $\Gamma > 0$. We will now use $T(h, \Gamma > 0)$ to test if the basic assumptions for the Unger model break down in the vibration dominated regime. We will find two flow regimes with the distinguishing features $T \sim \mu(\Omega)P$ and $T \not\sim \mu P$. We describe here how we can distinguish these regimes in the rheological data.

From Fig. 3.6(b-c) we see that that the flow curves for $\Gamma > 0$ all show significant rate dependence. Even so, we attempt to fit Unger's model to the rheological data. We thus fit $T(h, \Omega)$ to try to obtain a $\mu(\Omega)$. If this rate dependence were captured by an effective friction coefficient that depends only on Ω, with $T(h, \Omega) = \mu(\Omega)T_f(h)$, the rate dependence would lead to
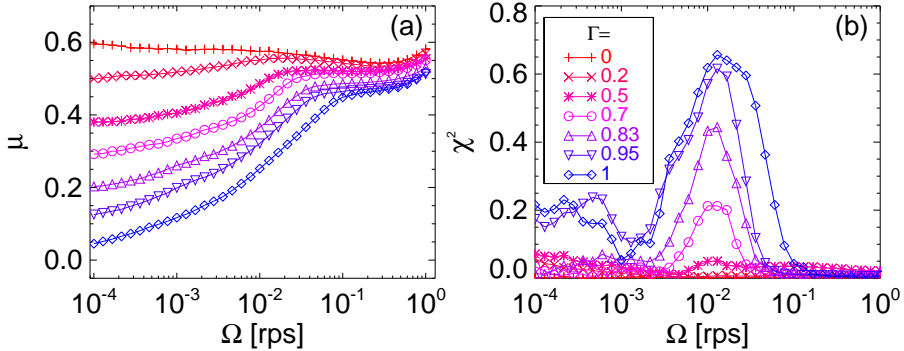
29

FIGURE 3.8: (a) The effective friction coefficient $\mu(\Gamma, \Omega)$ as found by fitting the data with Eq. 3.3. Instead of plotting an arbitrary, h-dependent, T, we now assign a dimensionless μ to each combination of Ω and Γ. As expected, the curves have similar shape as the traditional $T(\Omega)$ flow curves, indicating that μ decreases with increasing Γ and decreasing Ω. (b) The χ^2 of the fits, as defined in Eq. 3.4. There are two clear regions where the fit does not correspond well to the data.

a good fit of our data to the frictional model. To quantify the deviations between the data and fits to the frictional model, we calculate the best estimate of μ and the corresponding χ^2 as follows. For each fixed Ω and Γ, we have measured the torque for seven values of h, and then determine:

$$\chi^2 := \langle (\mu T_f(h) - T(h))^2 \rangle / \sigma^2_{T(h)} , \qquad (3.4)$$

where χ^2 is a standard measure to quantify the quality of a fit, and $\sigma^2_{T(h)}$ is the variance of $T(h)$. We apply this procedure for each value of Ω and Γ, and show the result for μ and χ^2 of these calculations in Fig. 3.8. For $\Omega > 0.3$ rps - the inertial regime - the fit works very well and results in a weakly rate-dependent μ, just as for $\Gamma = 0$. In addition, we find a large region for $\Gamma \leq 0.83$ and $\Omega < 0.5 \times 10^{-3}$ where the fit also works well, but this time with a more strongly rate-dependent effective fiction $\mu(\Omega)$. This tells us that even in this rate-dependent, vibration dominated regime, a frictional prediction is perfectly capable of describing the flow.

We do however observe two distinct regimes where χ^2 is large, indicating a poor fit. First, there is a significant peak in χ^2 around $\Omega = 10^{-2}$ rps for $\Gamma \geq 0.7$. Second, for $\Gamma \geq 0.95$ and $\Omega < 10^{-3}$ rps, χ^2 also is substan-
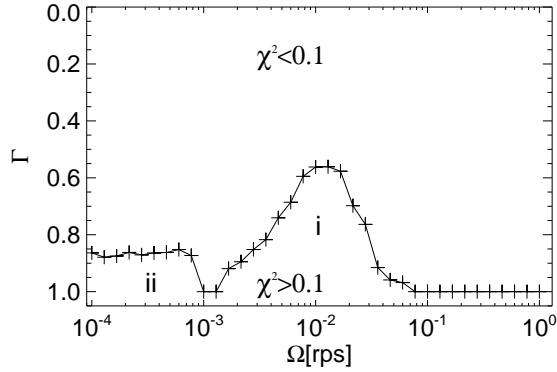
FIGURE 3.9: The boundary of $\chi^2 = 0.1$, where we interpolate $\chi^2(\Gamma)$ to find the location of the boundary. The two distinct regions where the data does not agree with $T_f(H)$ (i and ii) can clearly be seen. In the next sections we will see what causes the deviations from the frictional model in these two regimes.

tial. The two regimes are also clearly visible in Fig. 3.9 where we plot the boundary between a good fit ($\chi^2 < 0.1$) and a bad fit as a function of Ω.

The underlying physics in the two regimes is different. As we will show in the next section, the first peak is associated with a broad crossover regime between rate-dependent and rate-independent flows – a direct consequence of the flow profiles in the split-bottom geometry. The second peak we associate with a flow regime in which the rheology becomes pressure independent, as shown in Sec. 3.4.3.

Onset of Rate Dependence

The peak in χ^2 around $\Omega = 10^{-2}$ rps is consistent with the onset of rate dependence below $\Omega = 10^{-2}$ rps as per the following reasoning. First, both our raw data for T as well as the best fits for μ show that rate dependence sets in rather abruptly for $\Omega < 0.1$ rps, and that rate dependence is strongest for large Γ, consistent with the location and strength of the peak in χ^2. Crucially, this onset of rate dependence sets in at different flow rates for different heights (see Fig. 3.6), so that at a given Ω, the data for $T(h)$ mixes rate-independent and rate-dependent flows.

In Fig. 3.10(a) we show examples of T as function of height, that illustrate that when Ω enters this rate-dependent regime, $T(h)$ strongly de-
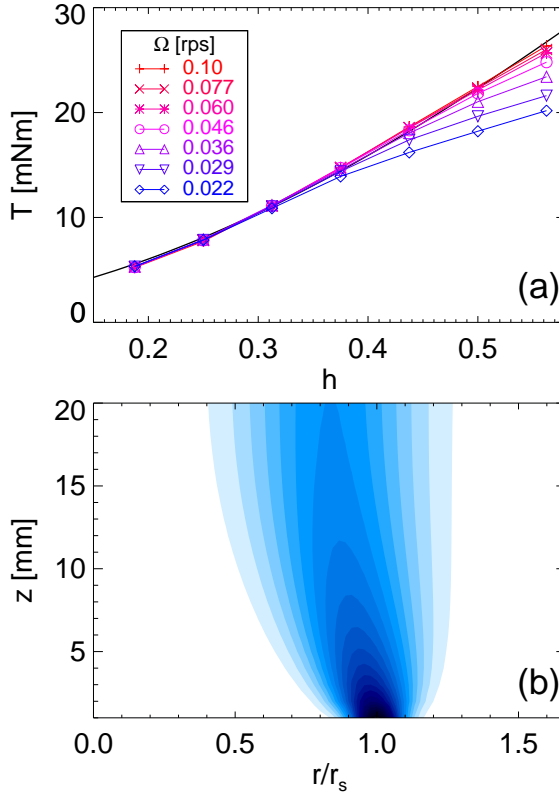
31

FIGURE 3.10: (a) $T(h)$ for $\Gamma = 0.95$ and a range in Ω at the point where the rate dependence starts. It can be seen that the curve drop for high h, resulting in an s-shaped $T(h)$ curve rather than an upwards curved T_f one. The black line is the fit with the frictional model to the top curve. (b) A theoretical prediction of $\dot{\gamma}/\Omega$ -which decreases with z- in the split-bottom cell [76, 85]. The color is scaled linearly from high $\dot{\gamma}/\Omega$ (dark) to low $\dot{\gamma}/\Omega$ (light).

viates from the quadratic form predicted by Eq. (3.3). To interpret this deviation, it is important to realize that at a given Ω, the local strain rate $\dot{\gamma}$ spans a wide range of values and has a strong z dependence [76, 85, 95] – see Fig. 3.10(b). Hence, as the torque T is an integral over the local stress in different layers in the material, $T(\Omega)$ mixes different local rheologies. More precisely: under the assumption that rate dependence sets in below a given $\dot{\gamma}$, there is a range of values of Ω for which the lower part of the sys-

tem (where strain rates are largest) is still rate independent, whereas the top part of the system (where strain rates are smallest) are already rate dependent. This is consistent with the "drop" in the $T(h)$ curves at large h shown in Fig. 3.10(a) – the deviations from the Unger model emerge first for large h, for which the range of strain rates is biggest and regime mixing is thus most pronounced. Our data also shows that once Ω is sufficiently low, so that all of the material is in a rate-dependent state, $T(h, \Omega)$ is close to $\mu T_f(h)$ so that χ^2 drops to low values again, and μ can be replaced with a rate-dependent $\mu(\Omega)$. The range of Ω over which this crossover exists broadens with Γ, since the rate dependence becomes stronger with Γ.

   In conclusion, the lowering of the friction coefficient μ and the peak in χ^2 around $\Omega = 0.01$ rps are caused by the onset of rate dependence which occurs at different Ω for different vertical locations in the flow cell. For $\Gamma \lesssim 0.8$, we also observe that once all the material is in the slow, rate-dependent regime, the fit to the frictional model achieves a low χ^2 again, so that $T(h, \Omega) \approx \mu(\Omega) T_f(h)$.

3.4.3 Fluidized Region

The growth of χ^2 for large Γ and low Ω signals a breakdown of the frictional picture, where shear stresses are proportional to the pressure, as we will describe in this subsection. To gain deeper insight in the flow phenomenology in this regime, we plot $T(h)$ for $\Gamma = 1$ and a range in Ω in Fig. 3.11. We see that for all filling heights the stresses drop with Ω, and at low Ω, $T(h)$ becomes approximately *linear*. The standard Unger model predicts a quadratic dependence of $T(h)$ on h, as mentioned above. A linear dependence would suggest a pressure-independent rheology, for which the increase of T with h is due only to increasing surface area on which the shear stress acts. Note that the large values of χ^2 here cannot be due to the existence of a crossover regime, as presented above for $\Omega \approx 10^{-2}$ rps. Evidence for this comes from Fig. 3.6(c), which shows that both rate dependence of $T(\Omega)$ is small, and that there is no strong difference in the rate dependence for different values of the height in this regime. First of all, that means that there is little mixing of different rheologies in the global torque signal; second, the rate dependence is weak, so even if there were some mixing, it would not produce a strong h dependence.
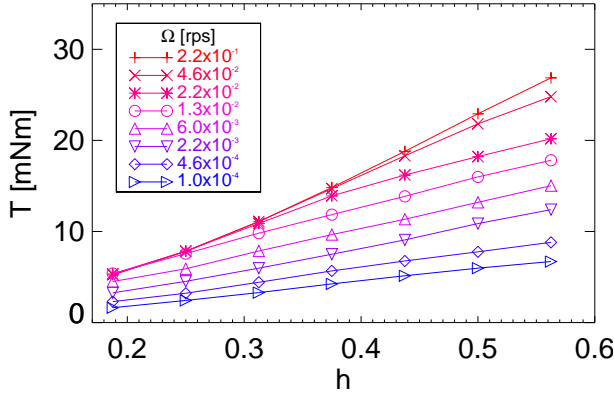
FIGURE 3.11: $T(h)$ curves for $\Gamma = 1$ and $\Omega < 10^{-3}$ rps. Towards lower Ω, the curves lose their curvature and become straight lines.

It it perhaps not surprising that new phenomena occur around the special value $\Gamma = 1$. For $\Gamma \approx 1$, the grains lose contact during part of the vibration cycle – the precise value of Γ where this happens depends on details [98, 99]. As a result, the confining pressure becomes zero during part of the cycle, and as most slip can be expected to occur when the normal grain forces are absent, the flows may become pressure independent, as in a viscous liquid.

Rate Dependent Flow Structure

Additional evidence for the loss of pressure dependence for high Γ and low Ω comes from measurements of the flow structure. From finite element calculations on the flow structure of a viscous liquid in the split-bottom geometry, it is known that the shear band is much closer to the center of the cell than for frictional flow [80]. As such, a pressure-independent rheology for the granular flows in this regime can be expected to be accompanied by similar changes in the flow structure.

To test this, we measured the velocity profiles $\omega(r)$ at the surface of our system for a range in Γ and Ω using particle image velocimetry [76–79]. In Fig. 3.12(a) we show examples of $\omega(r)$, showing a broadening and shift of the shear zones when Ω enters the pressure-independent regime. We
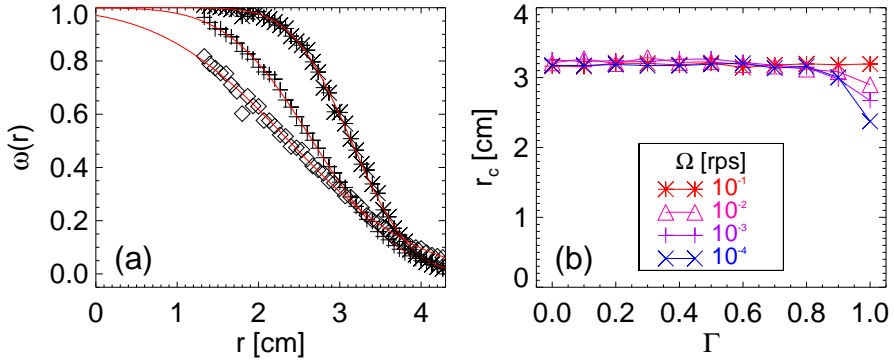
FIGURE 3.12: (a) $\omega(r)$ for $\Omega = 10^{-1}$ rps, $\Gamma = 0.2$ ($\times$), $\Omega = 10^{-3}$ rps, $\Gamma = 1$ (+), $\Omega = 10^{-4}$ rps, $\Gamma = 1$ ($\diamond$). In red, we add the fit with $\omega(r) = 1/2 - 1/2 \, \text{erf}[(r - r_c)/W]$. (b) The center of the shear band at the surface r_c as a function of Γ for $h = 0.47$ and Ω as indicated. For low Ω, r_c clearly decreases.

fit the velocity profiles with $\omega(r) = 1/2 - 1/2 \, \text{erf}[(r - r_c)/W]$, where r_c is the center of the shear band at the free surface [79].

In Fig. 3.12(b), we plot r_c for Ω ranging from 10^{-1} to 10^{-4} rps and a range in Γ. Clearly, the location of the shear band is mostly independent of Ω and Γ, including most of the rate-dependent regime. However, in the regime where we observed the pressure-independent rheology, we observe significant deviations in the flow profiles. The deviations show a trend towards a shear band moving inwards – consistent with the idea of a pressure-independent regime.

Moreover, we can modify the Unger model to test which rheological scenario is most compatible with the observed shift in the shear band. Throughout, we assume that the torque minimization principle is robust. The frictional torque model assumes $\sigma(z) \sim 1 - z/H$, in which the shear stress, being proportional to the hydrostatic pressure, goes to zero at the surface. We can replace this model with $\sigma(z) \sim 1 - (1 - \alpha_1)z/H$, in which the shear stress reaches a final value when approaching the free surface – see Fig. 3.13(a). The extreme case $\alpha_1 = 1$ represents a pressure-independent rheology. We compute the location of the shear band at the free surface as a function of model parameter α_1. The results are shown in Fig. 3.13(b). We find that for larger α_1, the location of the shear band at the free surface moves inwards. Thus, the closer the model resembles
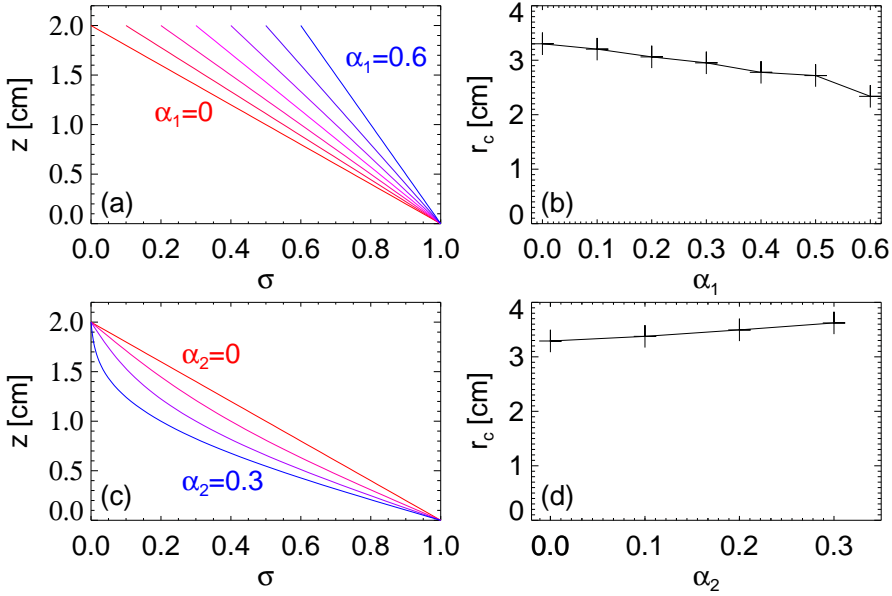
FIGURE 3.13: The center of the shear band at the surface, r_c, can be found using the method by Unger for given z-dependent stress $\sigma(z)$. In (a), we plot $\sigma(z)$ for case $\sigma(z) \sim 1 - (1 - \alpha_1)z/H$ where σ is still finite at $z = H$, in contrast to the frictional description where $\sigma(H) = 0$. The resulting r_c is shown in (b), we recover an inwards moving shear band as we observe in experiments. In (c) we plot $\sigma(z)$ for $\sigma = (1 - z/H) + \alpha_2 \sin[2\pi z/(2H)]$, where P and μ respectively vanish and decrease towards the surface, corresponding the a strain rate-dependent frictional picture, as we show in (d), this predicts an outwards moving shear band, contrary to what we observe.

a Newtonian rheology, the more the shear band moves towards the center. This can be understood intuitively as follows: the penalty for having a shear band at large radius at the surface is zero in the pressure-dependent model, because the shear stress goes to zero at the free surface. Once a finite amount of shear stress is present in the shear band at the surface, torque minimization will move the shear band inwards precisely as we observe in the experiments at $\Omega < 10^{-3}$ rps, $\Gamma > 0.9$.

Conversely, for a frictional, rate-dependent rheology, the shear stress closer to the surface is *lower* than that of a simple frictional model. We

model this with a $\sigma(z)$ that can be captured with:

$$\sigma = (1 - z/H) + \alpha_2 \sin[2\pi z/(2H)] \, , \qquad (3.5)$$

as shown in Fig. 3.13(c). The torque penalty for having a shear band at finite r is thus reduced, and the model predicts indeed an *increase* of the shear band radius at the free surface (Fig. 3.13(d)), contrary to what we observe. We thus conclude that our observation of the inward displacement of the shear band location at $\Omega < 10^{-3}$ rps, $\Gamma > 0.9$ is consistent with the granular flow obtaining a rheology which becomes pressure independent.

3.5 Conclusion

To summarize, we probe the rheology of weakly vibrated granular media and find several different flow regimes. First, for $\Omega > 0.3$ rps, our data shows the well-known *inertial flow* regime. In the absence of vibrations, lower flow rates lead to an essentially rate-independent, *quasi-static*, regime, where the variation of the torque is small, and where $T(h)$ is well fitted using Eq. (3.3), implying that the shear stresses are proportional to the pressure here. For $\Gamma = 0$, this regime covers all $\Omega < 0.1$ rps, whereas the range of flow rates where this rate-independent regime resides shrinks in the presence of vibrations, and almost vanishes for $\Gamma = 1$. For Ω below the rate-independent regime and $\Gamma > 0$, we have described three *vibration dominated* regimes. For two of these regimes, our data shows that the shear stresses are still proportional to the normal stresses, but now via rate-dependent $\mu(\Omega)$. For the slowest of these two regimes, we see a slow densification, leading to a kink in the flow curves. Finally, for Γ close to one, the vibrations affect the rheology of the granular medium so significantly, that the shear stresses are no longer proportional to the normal stresses, signifying a complete departure of the frictional nature that is a hallmark of all other types of slow granular flows.